The influence of Nickel on the corrosion protection of FeCrNi alloys after breakaway corrosion at 600 °C

Corrosion Science 240 (2024) 112473

Contents lists available at ScienceDirect

Corrosion Science

journal homepage: www.elsevier.com/locate/corsci

The influence of Nickel on the corrosion protection of FeCrNi alloys after breakaway corrosion at 600 °C

A. Persdotter [a,*], H. Larsson [b], J. Eklund [c], S. Bigdeli [d], T. Jonsson [a]

[a] Division of Energy and Materials, Chalmers university of technology, SE-412 96, Sweden
[b] KTH, SE-100 44, Sweden
[c] Valmet AB, SE-402 75, Sweden
[d] Höganäs AB, SE-263 83, Sweden

ARTICLE INFO

Keywords:
High temperature corrosion
Breakaway corrosion
Stainless steels
Nickel
Secondary corrosion protection
Internal oxidation

ABSTRACT

Breakaway corrosion of stainless steels remains a challenge for many industrial applications operating in harsh conditions. The lifetimes of metallic components are often determined by the corrosion propagation after breakaway. Nevertheless, studies on the protective properties of the Fe-rich oxides formed after breakaway are scarce. This study investigates the influence of Ni on the protection after breakaway on a broad range of Fe18CrxNi model alloys, by systematically inducing breakaway of the initially formed protective, Cr-rich oxides. The results clearly demonstrate an improved protection after breakaway for higher Ni-contents, explained by the alloys' ability to avoid internal oxidation involving Fe-rich BCC and spinel.

1. Introduction

High temperature corrosion remains a challenge for many industrial applications and is commonly addressed by the use of highly alloyed materials, such as stainless steels. The corrosion protection of stainless steels is considered to be dependent on the formation of a protective Cr-rich, corundum-type oxide [1,2], also known as the primary corrosion protection [3]. However, in harsh corrosive environments this Cr-rich oxide barrier tends to break down, resulting in an accelerated growth rate caused by the formation of a less protective multi-layered Fe-rich oxide scale, a well known process referred to as breakaway corrosion [4–26]. Thus, in order to meet current, and future, corrosion challenges in harsh environments, a materials ability to resist corrosion after breakaway, i.e., its secondary corrosion protection, is important to study. The ability to withstand corrosion after breakaway is in principle already at play in many applications, where the selection of alloys and prediction of material lifetimes is based, to a large extent, on empirical knowledge. However, the explanation to the difference in corrosion rate and mechanistic understanding thereof is not completely understood. One example is in power plants for combustion of biomass and waste, where stainless steels positioned in the superheater region may sustain for several years in operation, even though the harsh environment (rich in alkali/water vapor) is known to rapidly induce breakaway of these materials [27–29].

Corrosion of stainless steels exposed under conditions inducing breakaway corrosion has previously been studied by several authors [8, 11,25,26,29,30]. These studies have mainly focused on the breakaway event and how to prevent breakaway corrosion, i.e., retaining the primary corrosion protection. Previous research, focused on the initiation/breakaway event, indicate a similar microstructure obtained after the onset of breakaway of Fe-based alloys, seemingly independent of suggested breakaway-reaction [8,20,22,29,31]. The oxide scale formed has previously been studied in a variety of environments (Air+H_2O [8,31], Ar+H_2O [31], N_2+O_2+H_2O [19,24,26,32], Ar+O_2+H_2O [22], Ar+CO_2 [20], Ar+CO_2+H_2O [20], Ar+H_2O+H_2 [26, 29], N_2+O_2+H_2O+KCl [29,32,33], N_2+O_2+K_2CO_3 [3,29,33], N_2+O_2 +H_2O+KCl+SO_2 [29]. Regardless of the environments studied, the oxide scales have been composed of an outward-growing almost pure Fe oxide, and an inward-growing oxide with a more complex microstructure and varying composition. Recent studies have shown that the growth rate of this multi-layered oxide scale may be altered by the change in alloy composition [3,33–35], explained by other factors than those determining the alloys' ability to withstand breakaway corrosion and the Cr-rich primary protection, as formed before breakaway. Thus, insight to the effect of alloying elements, such as e.g., Ni, on the multi-layered Fe-rich oxides formed after breakaway, i.e., the secondary corrosion protection, is an important topic that has not yet been studied in a systematic way.

This study investigates the influence of Ni on the secondary corrosion protection (Fe-rich oxide) of a wide set of Fe18CrxNi model alloys with varying amounts of Ni (x = 0–82 wt%). To systematically

* Corresponding author.
E-mail address: amanda.persdotter@chalmers.se (A. Persdotter).

https://doi.org/10.1016/j.corsci.2024.112473
Received 21 December 2023; Received in revised form 22 August 2024; Accepted 19 September 2024
Available online 23 September 2024

Table 1
Nominal composition (wt%), grain size (μm) and crystal structure for the investigated model alloys.

Alloy	Cr	Ni	Fe	Grain size (alloy)	Crystal structure*
Fe18Cr	18	0	82	150	Ferrite (BCC)
Fe18Cr2Ni	18	2	80	90	Ferrite (BCC)
Fe18Cr10Ni	18	10	72	60	Austenite (FCC)
Fe18Cr20Ni	18	20	62	60	Austenite (FCC)
Fe18Cr34Ni	18	34	48	70	Austenite (FCC)
18Cr82Ni	18	82	–	–	Austenite (FCC)
Fe2.25Cr	2.25	0	97.75	–	Ferrite (BCC)
Fe10Cr2Ni	10	2	88	–	Ferrite (BCC)

investigate the effects of alloying elements on the secondary corrosion protection, this study focuses on short exposure times under simplified conditions. This is in order to limit the risks of oxide spallation, and avoid possible effects of corrosive species, such as e.g., Cl, known to accelerate corrosion by mechanisms that may vary for different alloying elements. The investigated alloys are enforced to undergo breakaway corrosion by the addition of potassium carbonate (K_2CO_3(s)) and are exposed in oxidizing conditions at 600 °C. K_2CO_3(s) has previously been shown to induce breakaway corrosion by Cr-depletion of the primarily formed Cr-rich oxide scales [18]. Thus, the use of K_2CO_3(s) allows for a systematic study of the secondary corrosion protection, without the influence of other corrosive species, such as e.g., chlorides or water vapor. Besides the mechanistic investigation of the influence of Ni, the results in this study may also act as a reference to study the effects of other corrosive species on FeCrNi alloys after breakaway. The study combines thermogravimetric data, microstructural investigation and thermodynamic calculations in order to increase the understanding of the secondary corrosion protection FeCrNi-alloys at intermediate temperature.

2. Experimental procedure

A broad range of FeCrNi model alloys (0–82 wt% Ni) were investigated in order to systematically study the influence of Ni on the secondary corrosion protection of stainless steels (i.e., protection after breakaway), see Table 1. For comparison, two low alloyed model alloys were also exposed (see Fe2.25Cr and Fe10Cr2Ni in Table 1). All investigated alloys were known to form a slow growing, Cr-rich corundum-type oxide in mildly corrosive environments (e.g. dry air) at 600 °C (the primary corrosion protection) [3]. The influence of Ni was investigated both on ferritic(BCC) and austenitic(FCC) FeCrNi-alloys. All alloys were exposed at 600 °C under a controlled oxidizing atmosphere (5%O_2 + 95%N_2), with samples positioned parallel to the gas flow, for up to 168 h. Breakaway corrosion was induced by the application of 1 mg/cm^2 K_2CO_3(s) on the samples surface prior to exposure. The formed oxide scale microstructures were analyzed in cross section and characterized by scanning electron microscopy and energy dispersive X-ray spectroscopy. The experimental results were combined with thermodynamic calculations in order to better explain the observed influence of Ni.

2.1. Sample preparation

The model alloys were produced at Kanthal AB by induction heating and casting in a copper mold under an Ar-atmosphere. For details regarding production of the model alloys, see [3]. The complete material-matrix is summarized in Table 1 including composition, alloy grain size and crystal structure. The alloy grain sizes were investigated by light optical microscopy (LOM) on chemically etched samples. The chemical etching of the Fe18Cr alloy was performed at 60 °C in a solution of HCl/H_2O (50:50), while the etching of all the FeCrNi model alloys was performed in HCl/HNO_3/H_2O (45:45:10) above 60 °C.

The received model alloys were cut into coupons with sample dimensions 11 × 11 × 2 mm for the tube furnace exposures and 8 × 10 × 2 mm for the time-resolved thermobalance exposures. Prior to exposure, the samples were ground with SiC paper (P500-P4000) and subsequently polished with 3 and 1 μm diamond suspension to mirror-like appearance. The samples were degreased in acetone using ultrasonic agitation.

The investigated alloys were enforced to undergo breakaway corrosion by the addition of 1 mg/cm^2 K_2CO_3, deposited onto the polished samples prior to exposure by spraying a saturated aqueous solution of the salt. The salt was left to react with the sample during exposure and was not manually removed at any point. Gravimetric measurements were made using a Sartorius balance with microgram resolution. The samples were subsequently dried in air and stored in a desiccator prior to exposure and awaiting post-exposure analysis to avoid atmospheric corrosion.

Wide cross sections of the exposed samples were prepared by Broad ion beam (BIB) milling in order to study the microstructure of the oxide scales formed after breakaway. The BIB used in this study was a Leica EM TIC 3X BIB equipped with a triple Ar ion gun operated at 8 kV. Prior to milling, the steel coupons were sputtered with gold, covered by a Si-wafer and subsequently cut, without lubrication, using a low speed saw.

2.2. Exposures

All alloys were exposed in mild, oxidizing conditions (5% O_2 + 95% N_2) at 600 °C. The atmosphere was chosen to study simple oxidation after breakaway (i.e., the secondary corrosion protection, initiated by the presence of K_2CO_3), since these conditions are previously known to result in a primary corrosion protection in the absence of K_2CO_3 [3]. A minimum of three samples of each model alloy were exposed for each furnace setup. All alloys were exposed for 168 h in a horizontal tube furnace (flowrate: 3 cm/s) to compare the influence of Ni on the oxide growth rate, as well as 48 h in a Setaram Setsys thermobalance (flowrate: 1.5 cm/s) to record the oxidation kinetics by thermogravimetric analysis (TGA). The samples were positioned in parallel to the direction of the gas flow in both furnace setups (i.e., standing vertically in the tube furnace and hanging vertically in the thermobalance).

Estimated oxide scale thicknesses, x, were calculated from mass gain data, W [g/cm^2], in order to compare with measured oxide scale thicknesses, according to Eq. (1):

$$x = W \times F = W \times \frac{1}{\rho}\left[\frac{bM_O}{bM_O + aM_M}\right], \quad (1)$$

where x is the oxide thickness, W is the weight gain, F is the multiplying factor used to only account for the uptake of oxygen, ρ is the oxide density, and M_O and M_M are the molar weight of oxygen and metal in a M_aO_b oxide. The calculations were performed assuming that the oxide scales were dense, composed of one predefined oxide (M_aO_b) and that the measured mass gain is a result only of oxygen uptake from the atmosphere. The predefined oxide was chosen to be Fe_3O_4 for all oxides since the resulting multiplying factor(F) in Fe_3O_4 is similar to both $FeCr_2O_4$ and NiO ($F_{Fe_3O_4} = 1.4284 \approx F_{NiO} = 1.4280$), thus covering the majority of the oxides expected to form. The choice was made also to keep all data directly proportional to mass gain, to allow for comparison with other studies and the thermobalance exposures.

2.3. Analytical techniques

The oxide scales were imaged and analyzed by scanning electron microscopy and Energy dispersive X-ray spectroscopy (EDX). The instruments used was an FEI Quanta ESEM 200, operated in high vacuum mode, and a Zeiss Ultra 55 FEG SEM, both equipped with a field emission gun and an EDX detector for chemical analysis. The microscopes were operated at an accelerating voltage of 10–20 keV for BSE imaging

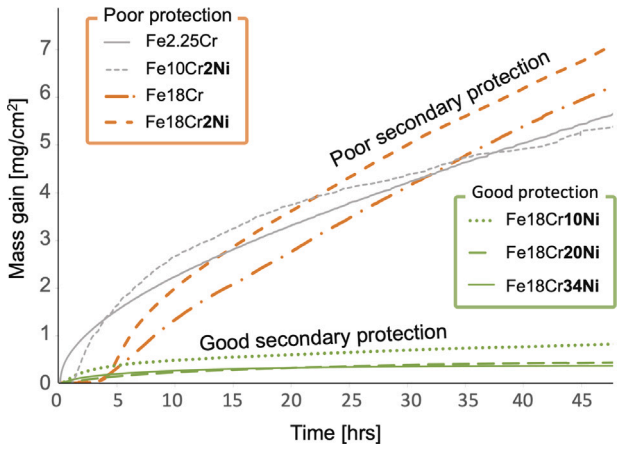

Fig. 1. Thermogravimetric analysis for FeCrNi model alloys exposed for 48 h in 5% O_2 + 95% N_2 at 600 °C with K_2CO_3(s) deposited prior to exposure in order to break down the primary protection.

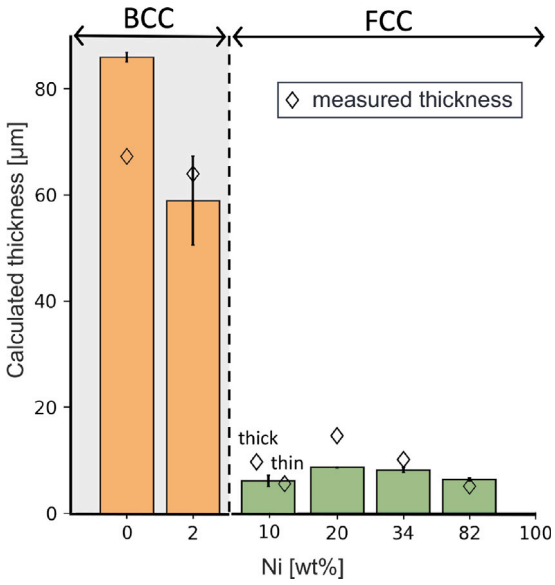

Fig. 2. Calculated and measured (◇) thicknesses of oxide scales formed on FeCrNi model alloys exposed for 168 h in 5% O_2 + 95% N_2 at 600 °C in exposure to K_2CO_3(s).

and chemical analysis in the FEI Quanta as well as 1.5–2.5 keV for higher resolution in the Zeiss Ultra. Both secondary electrons (SEs) and backscattered electrons (BSEs) were used for imaging, but only BSE-images are shown in this paper. The compositions, as measured by EDX analysis in this study, are reported in cationic percentages (cat%), excluding oxygen in the quantification due to large errors associated with oxygen quantification in EDX-analysis.

2.4. Thermodynamic calculations

Thermodynamic calculations were carried out using the Thermo-Calc software [36] with databases TCFE9 and TCOX11. Note that the phase diagrams were calculated with a total fixed amounts of Ni for each region. Hence, the composition of each phase in the two- and three-phase regions cannot be extracted visually from the diagrams. Point equilibrium calculations were performed in selected regions to extract composition of each phase in multi-phase regions.

3. Results

3.1. Oxidation kinetics

Fig. 1 shows the oxidation kinetics of the investigated FeCrNi model alloys during 48 h of exposure. Reactive alkali was deposited on the surface to systematically induce breakaway corrosion. The incubation times to breakaway were similar and comparatively short for all investigated alloys. From Fig. 1 it is obvious that the amount of Ni in the alloy has a large influence on the oxide growth rate after breakaway. The alloy containing 2 wt% Ni (Fe18Cr2Ni) grows at a similar rate as the binary Fe18Cr (containing no Ni), which is comparable to the oxide growth rates of the low alloyed steels Fe2.25Cr and Fe10Cr exposed under the same conditions. As the level of Ni is further increased the oxidation rates decline rapidly, suggesting a transition from poor- to good secondary corrosion protection. Note that the Ni-base alloys, 18Cr82Ni was not exposed in the thermobalance, since the main scope of this study is the influence of Ni in FeCrNi alloys.

Fig. 2 shows the calculated thicknesses of the oxide scales formed on the model alloys after longer exposures (168 h). The calculations were based on mass gain data, assuming the formation of a dense Fe_3O_4 oxide scale. The calculated thicknesses are in good agreement with the measured oxide scale thicknesses and the trends observed after 48 h of exposure. It is obvious that the secondary corrosion protection of FeCrNi alloys is influenced by the amount of Ni in the alloy, with oxides growing approximately 10 times slower after a certain amount of Ni is reached. However, no significant difference in growth rate is observed for higher Ni contents, in good agreement with the short thermobalance exposures.

From these results, the FeCrNi alloys may be divided into two categories: alloys forming fast-growing, poorly protective oxides (≤2%Ni) and alloys forming slow-growing oxides after breakaway (>2%Ni), i.e., forming a good secondary corrosion protection. Thus, the results indicate that the minimum amount of Ni required to form a slow-growing, good secondary protection is between 2 and 10 wt% for Fe18CrxNi alloys. It should be noted that the increased amount of Ni in the alloy (0 to 82%Ni) results not only in a different alloy composition, but also a change in crystal structure of the alloy matrix (from ferritic(BCC) to austenitic(FCC), see Table 1). Note that the difference in growth rate is not directly correlated to the alloy grain size, which remained similar for e.g. the austenitic alloys and ferritic Fe18Cr2Ni (see Table 1).

3.2. Oxide microstructure

The two different types of multi-layered Fe-rich oxides (fast- and slow-growing) are shown in Fig. 3, represented by a selection of FeCr(Ni) alloys exposed for 48 h. Fig. 3a–b represent the fast-growing, non-protective oxides, while 3c–d represents the slow-growing, protective oxides. The microstructure and composition of the oxides formed after both 48 and 168 h were analyzed in cross section SEM/EDX, as summarized in Tables 2 and 3. In general, the outward-growing scales formed on all the Fe-based model alloys were composed of almost pure Fe oxide (Fe_2O_3/Fe_3O_4), while the inward-growing scales were mixed and consisted of Fe, Cr and Ni in varying amounts depending on alloy composition (see Table 3). Moreover, an internal oxidation zone (IOZ) was apparent on all alloys (see Fig. 3).

3.2.1. Poor secondary corrosion protection

The two alloys representing the fast-growing, poorly protective oxide category (Fe18Cr, Fe18Cr2Ni) obtained similar oxide scale thicknesses and microstructure (see Fig. 3a–b and Table 2). The Fe18Cr formed an oxide scale composed of 60%–62% outward-growing and 38%–40% inward-growing oxide, whereas the oxide formed on the Fe18Cr2Ni alloy was composed of 55%–60% outward-growing and 40%–45% inward-growing oxide. The thickness of the outward-growing scale formed on Fe18Cr2Ni remained constant throughout

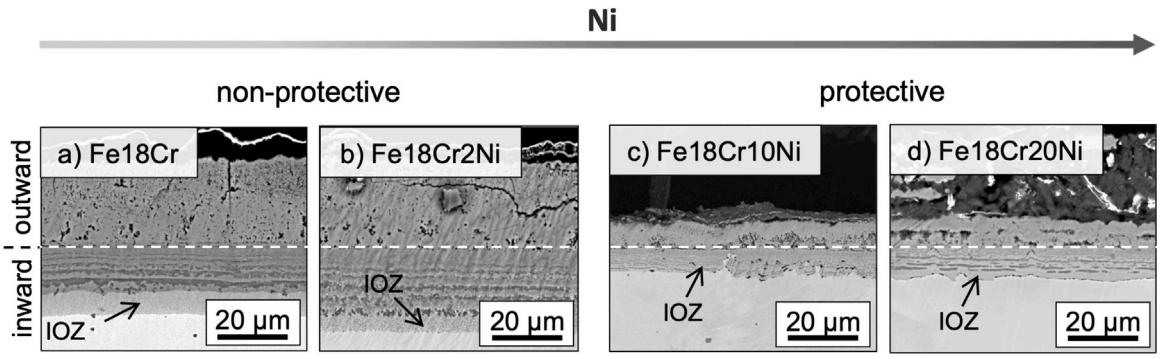

Fig. 3. SEM-BSE image of the oxide scales formed on a selection of FeCrNi model alloys after 48 h of exposure. The selection was made in order to illustrate the similarities within the same type of oxide (non-protective vs. protective), and the obvious difference in growth rate between the two types. The inward-growing scales exhibit a periodic microstructure with alternating fully oxidized segments (see bands of dark/bright contrast in the BSE-images). Note that the fully oxidized regions in a–b are associated with the brighter contrast (dark = pores, bright = oxide), whereas the fully oxidized segments in c–d are associated with the darker contrast (dark = oxide, bright = FeNi-FCC dispersed in oxide).

the sample surface whereas the thickness of the inward-growing scale varied depending on the analyzed region. The outward-growing scale formed on both alloys were composed of almost pure Fe oxide, while the composition detected in the inward-growing scales resulted in cationic ratios similar to the unexposed alloy after removal of Fe to grow the outward-growing scale.

The inward-growing scales of the poorly protective oxides (Fe18Cr and Fe18Cr2Ni) exhibited a periodic microstructure with alternating fully oxidized segments (see bands of dark/bright contrast in Fig. 3a–b). Note that the fully oxidized regions in 3a–b are associated with the brighter contrast segments, whereas the dark regions are associated with a porous oxide segment. The dense, fully oxidized, segments of the inward-growing scales were almost identical in composition for the poorly protective scales, containing approximately 60 at% Fe and 40% Cr (+4% Ni in Fe18Cr2Ni), reported for cations, see Table 3.

3.2.2. Good secondary corrosion protection

Two alloys representing the slow-growing, protective oxide category, Fe18Cr10Ni and Fe18Cr20Ni, are shown in Fig. 3c–d. These oxide scales were similar in thickness on the majority of the sample surfaces. The scale thickness varied slightly more on the Fe18Cr20Ni alloy as compared to the Fe18Cr10Ni after 48 h, while the opposite trend was observed after 168 h of exposure.

The oxide scales formed on the alloys exhibiting a good secondary corrosion protection were composed of ~50%–60% outward-growing and ~40%–50% inward-growing oxide scale, with indicated larger relative amounts of inward-growing scale for higher Ni contents (see Table 2). The Fe18Cr10Ni alloy exposed for 168 h formed both thin (~6 µm) and thick (~10 µm) oxide regions. The thin oxide regions were composed of 65% outward-growing and 35% inward-growing oxide scale, whereas the thick oxide region (~10 µm) contained 60% outward-growing and 40% inward-growing oxide scale.

The inward-growing scales adopted a periodic microstructure with alternating fully oxidized segments (see bands of dark/bright contrast in Fig. 3c–d). However, in contrast to the poorly protective oxides, the fully oxidized segments in Fig. 3c–d are associated with the darker BSE-contrast. This is explained by that the fully oxidized segments formed on the poorly protective oxides are alternated between porous segments (dark = pores, bright = fully oxidized), whereas the fully oxidized segments formed on the alloys exhibiting good protection (Fig. 3c–d) are alternated between segments rich in FeNi-rich FCC-metal (dark = fully oxidized, bright = FeNi-FCC dispersed in oxide).

The chemical composition of the fully oxidized segments were similar for the oxides exhibiting a good secondary corrosion protection, containing approximately 40 at% Fe, 40% Cr, and 20% Ni (reported for cations), see Table 3. By comparing this composition to that of the unexposed alloys (after removal of Fe to grow the outward-growing scale) it may be noted that Ni/Cr ratios are lower than the unexposed alloy on the alloys forming a good secondary corrosion protection (e.g., Fe18Cr10Ni, Fe18Cr20Ni). This is expected, since a substantial amount of FeNi-metal was dispersed within the oxide, in particular in the segments that was not fully oxidized (see the bright contrast regions in the BSE-image in Fig. 4c–d). Thus, a large amount of Ni remains in the metallic FeNi-regions observed. Note that the composition reported from EDX-analysis of the segments that are rich in metallic FeNi ('M+O' in Table 3) are averages from both the FeNi-metal and the surrounding oxide.

Fig. 4 shows a close-up of the microstructure of the inward-growing scale and metal/oxide interface on an alloy exhibiting (a) poor secondary protection (Fe18Cr2Ni) and (b) good secondary protection (Fe18Cr10Ni) after 48 h of exposure. As previously discussed, the microstructure is non-homogeneous containing fully oxidized regions, metallic regions as well as pores (of similar dimensions as the metallic regions) dispersed in the surrounding oxide. The spatial resolution of SEM/EDX is not sufficient to obtain the composition of each region separately in the non-homogeneous inward-growing scales. However, the average composition in the multi-phase region remains useful to study the system by equilibrium calculations, which is done in the discussion below. Nevertheless, the compositions detected are reported in Table 3. It may be noted that a few percents of potassium were detected in some of the oxide scales. However, the localization to pores suggests that this was due to sample preparation and that potassium is spread to this region from the surface. Further studies are required to conclude with certainty whether or not the detected potassium has been involved in the growth process.

4. Discussion

4.1. Influence of Ni

Previous studies have shown that an increased amount of Ni is beneficial for the primary protection and the mitigation of breakaway corrosion (see e.g. [5,8,26,37,38]). From the results in this study it is obvious that the amounts of Ni in the alloy has a great influence on the oxide growth rates also *after* breakaway. The results clearly indicate a diffusion-controlled mechanism after breakaway (see Fig. 3). The microstructural investigation suggests that the reduced growth rates are explained by a reduced diffusion rate through the inward-growing part of the multi-layered Fe-rich oxide scales, as formed on all alloys. The incubation times to breakaway were similar and comparatively short for all investigated alloys. Thus, the incubation time to breakaway is concluded not to be the explanation to the difference in growth rates observed as the amount of Ni in the alloy was increased. The FeCrNi alloys formed oxide, significantly more slow-growing, after a

Table 2
Summary of the oxide scale microstructure formed on FeCrNi model alloys with varying amounts of Ni after 48 h and 168 h of exposure in 5%O_2 + 95% N_2 at 600 °C in the presence of K_2CO_3 (average and (range)). Left to right: Calculated thickness, measured oxide scale thicknesses, relative amounts of inward- and outward-growing scales and oxide grain sizes. Due to difficulties in separating hematite and magnetite in the micrographs the grains reported in the outward-growing scale are assumed magnetite grains.

Alloy	Thickness					Grain size	
48 h	Calculated [μm]	Measured [μm]	Outward [μm]	Inward [μm]	Out:in [%:%]	Outward [nm]	Inward [nm]
Fe18Cr	–	37	23	14	62:38	1000	–
Fe18Cr2Ni	–	45	26	19	58:42	1000	–
Fe18Cr10Ni	–	17	9	8	53:47	150	100
Fe18Cr20Ni	–	16	8	8	50:50	200	–
Fe18Cr34Ni	–	–	–	–	–	–	–
168 h							
Fe18Cr	86	67 (65–73)	40	27	60:40	1000	–
Fe18Cr2Ni	59	64 (57–68)	36	28	60:40-55:45	–	–
Fe18Cr10Ni	6	6 (6–10)	4–6	2–4	thin 65:35	–	–
					thick: 60:40	–	–
Fe18Cr20Ni	9	15 (15–21)	9	6	60:40-50:50	–	–
Fe18Cr34Ni	8	10 (5–10)	3–5	2–5	60:40-50:50	–	–
18Cr82Ni	6	5 (5–6)	2–3	2–3	40:60-50:50	–	–

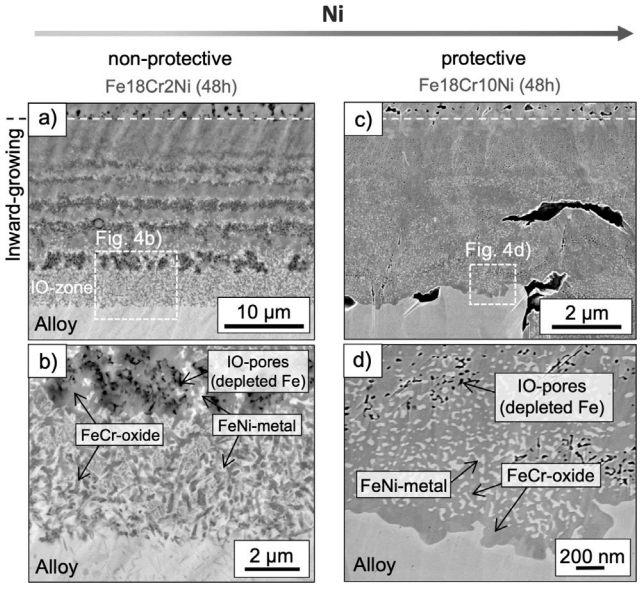

Fig. 4. SEM-BSE image of the inward-growing scale and IOZ formed on; a–b: one alloy forming a poorly protective oxide (Fe18Cr2Ni), and c–d: one alloy considered to form a good secondary protection (Fe18Cr10Ni).

Table 3
Approximate compositions [at%] (reported for cations) of the inward-growing oxide scales formed on the Fe18CrxNi model alloys after 48 h and 168 h of exposure in 5%O_2 + 95% N_2 at 600 °C in the presence of K_2CO_3(s). Note that the measurements are performed on the dense oxide segments (see Fig. 3. Bright contrast in Fe18Cr + Fe18Cr2Ni = Fully oxidized, dark contrast in Fe18Cr10Ni + Fe18Cr20Ni = Fully oxidized).

48 h	Fe [at%]	Cr [at%]	Ni [at%]
Fe18Cr	60	40	0
Fe18Cr2Ni	59	38	3
Fe18Cr10Ni	45–50[a]	35–40[a]	10-20[a]
Fe18Cr20Ni	35–40 (M + O:29–32[a])	45 (M + O:29–30[a])	15–20 (M + O:39–42[a]),
168 h			
Fe18Cr	59	41	0
Fe18Cr2Ni	58	38	4
Fe18Cr10Ni	40	40	15–20
Fe18Cr20Ni	40 (M + O:30–31[a])	40 (M + O:30–31[a])	20 (M + O:38–40[a])
Fe18Cr34Ni	15–20[a]	30–35[a]	45–55[a]
18Cr82Ni	–	25[a]	75[a]

[a] The oxide segments rich in FeNi-metal (M + O) are measured in regions covering both fully oxidized regions and FeNi-metal dispersed in the surrounding oxide.

certain amount of Ni was reached. However, no significant differences in growth rates were observed when further increasing the Ni content. The difference in growth rate clearly demonstrated a separation into poor (≤2%), and good (≥10%) secondary corrosion protection as the amounts of Ni was increased. Note that the minimum amount of Ni required to form a slow-growing, good secondary protection may be between 2 and 10 wt% for the Fe**18Cr**xNi alloys investigated.

From the growth rates observed in this study it may appear as if the Ni-content plays an insignificant role in the secondary corrosion protection after a certain amount of Ni has been reached. However, looking into the activity of Cr in the alloy (Fig. 5) and how it changes at elevated Ni contents opens up another aspect of the influence of Ni. Fig. 5 shows the activity of the key oxide forming elements (Cr and Fe) as a function of Ni (wt%) in the austenitic alloy at 600 °C, calculated using Thermo-Calc software. The Cr and Fe activities remain similar for Ni contents between 5–15 wt% (see Fig. 5a) for the Fe10CrxNi alloy. However, Fig. 5b, as calculated for Fe18CrxNi, demonstrate that the amount of Ni in the alloy has a great influence on the activity of both Cr and Fe for the alloy containing more Cr. The results suggest that the activity of Cr increases significantly while the activity of Fe decreases for higher Ni contents, indicating that a higher Ni contents would promote the formation of a Cr-rich oxide scale. Thus, an increased amount of Ni may accelerate the transition into a Cr-rich corundum-type oxide scale below the outward-growing Fe-oxide scale. The suggestion is strengthened by a recent study by Ssenteza et al. [35] that observed the formation of a thick (~ μm) Cr-rich corundum-type oxide, formed in the position of the inward-growing spinel (underneath the outward-growing Fe-rich oxide) on a high Cr- and Ni-containing stainless steel (27Cr33Ni3Mo) exposed in the presence of KCl(s) for longer durations (1000–8000 h).

4.2. Poor- vs. good secondary protection

Overall, the microstructural investigation performed in this study suggests that the oxide scale growth is diffusion controlled for all the FeCrNi alloys studied. The oxide scales formed after breakaway were composed of clearly separated outward- and inward-growing oxides. The outward-growing scales formed on all the Fe-based model alloys were composed of almost pure Fe-oxide, while the inward-growing scales were mixed and consisted of Fe, Cr and Ni in varying amounts depending on the model alloy, see Table 3. The Ni-base alloy (18Cr82Ni) formed an outer almost pure nickel oxide (NiO) and an inner mixed

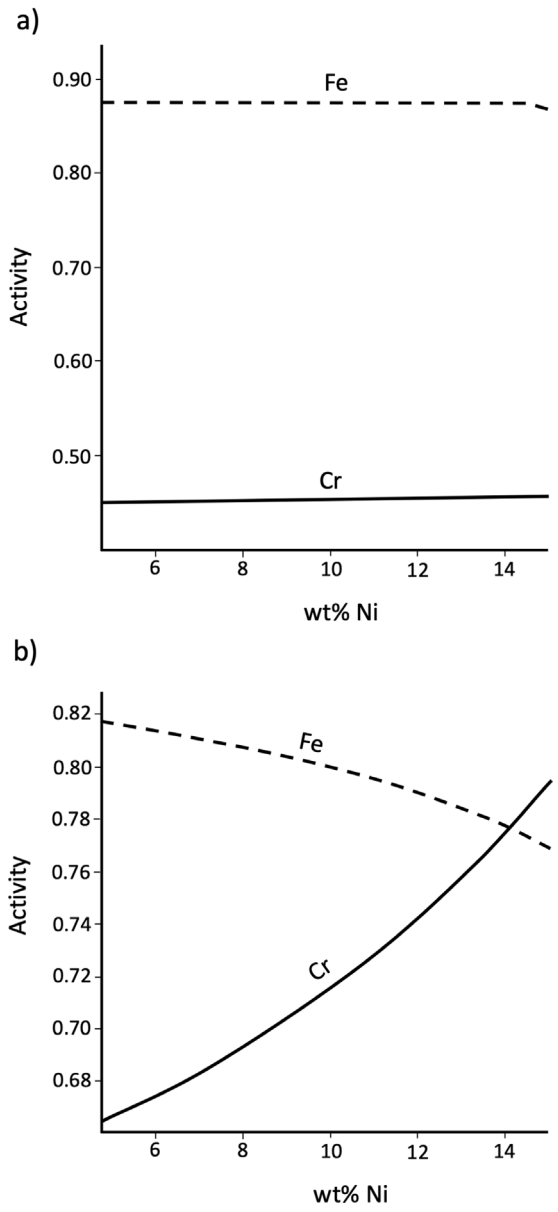

Fig. 5. Activity of Cr and Fe in an austenitic alloy at 600 °C as a function of Ni-content for (a) Fe10CrxNi and (b) Fe18CrxNi.

NiCr-oxide. The relative amounts of inward- and outward-growing scale was approximately 60% outward-growing and 40% inward-growing for all oxide scales, but with a slight increase for higher Ni-contents on the alloys exhibiting a good secondary corrosion protection (see Table 2). This could possibly be explained by a reduced outward-diffusion of Fe, resulting in a higher relative amount of inward-growing scale.

The microstructure of the inward-growing oxide formed on both the alloys exhibiting poor- and good secondary protection was non-homogeneous containing fully oxidized regions, metallic regions as well as pores (of similar dimensions as the metallic regions) dispersed in the surrounding oxide. This is in good agreement with previous studies [24–26,31], indicating that both these type of oxides have grown in part by internal oxidation.

The inward-growing scale of the poorly protective oxides (Fe18Cr and Fe18Cr2Ni) were composed of alternating dense and porous layers, which was not observed on the alloys exhibiting good secondary protection. The porous segments were recently suggested to form by rapid consumption Fe [33], resulting in dense oxide segments (Cr-rich spinel), and porous oxide segments composed of pores within a network of Cr-rich spinel. Thus, the pores observed in this study are interpreted to be remnants of the rapid consumption of Fe (from Fe-rich BCC-metal in the IOZ).

4.3. What determines the secondary corrosion protection in FeCrNi-alloys?

The general aspects of the secondary corrosion protection was previously investigated by Persdotter et al. [3]. Eklund et al. [33,34] studied the secondary corrosion protection on FeCrAl alloys and suggested that internal oxidation was the main reason for the fast oxide growth rates observed on several alloys after breakaway. It was suggested that the internal oxidation, resulting in the formation of Cr-rich spinel precipitates in a Cr-depleted (i.e., Fe-rich) metallic matrix, would result in that the available metallic Fe would be consumed to form an outward-growing scale, resulting in overall growth rates similar to pure Fe. Thus, the secondary corrosion protection of FeCrAl alloys was suggested to be mainly determined by the ability to escape internal oxidation. Thus, the results from this study will here be discussed by means of thermodynamics to investigate the influence of Ni on the stability regions for internal oxidation in FeCrNi alloys.

Fig. 6a shows a phase diagram for the FeCrO system obtained at 600 °C, where S_x are spinel oxides, C_x are corundum type oxides and BCC and FCC metallic phases. The stability region for the IOZ containing Fe-rich BCC metal is indicated in gray, at partial pressures of oxygen relevant the corrosion front ($10^{-30} < pO_2 < 10^{-25}$). Fig. 6b–e shows a cut-out of this region for different fixed amounts of Ni (b: 2%Ni, c:6%Ni, d:10%Ni, e:15%Ni) to illustrate how Ni would influence the stability region of this type of internal oxidation. From Fig. 6 it is obvious that an increased amount of Ni shifts the stability region towards the left, reducing the amount of Cr needed to escape this type of internal oxidation. However, the stability region for 'FCC+S_{Cr}'-internal oxidation remains almost unaffected by the addition of Ni. Hence, the transition form poor- to good secondary corrosion protection observed in this study, may not be explained by internal oxidation in general, but is suggested to be caused by the onset of a specific internal oxidation containing Fe-rich BCC, hereinafter referred to as the *detrimental internal oxidation* (D-IO).

The average composition of the inward-growing oxides, as measured by means of EDX-analysis in this study (see Table 3), allows us to test the hypothesis of the D-IO-region. The composition of the oxide scale formed on one alloy exhibiting poor (Fe18Cr2Ni), as well as good (Fe18Cr10Ni), secondary corrosion protection are marked in Fig. 6 for illustration. The phase diagrams indicate that Fe-rich BCC, Cr-rich spinel (S_{Cr} = 67 cation%Cr) and Fe-Ni FCC would form on the poorly protective Fe18Cr2Ni-alloy, whereas a Cr-rich spinel (S_{Cr}) and FeNi FCC-metal would form on the alloys exhibiting a good secondary corrosion protection (e.g. Fe18Cr10Ni). This is in good agreement with previous studies performed with STEM/EDX on commercial Fe18Cr10Ni alloys [26] with an almost identical microstructure as observed in the present study. Note that the Ni-content of the oxides formed on e.g. Fe18Cr20Ni and Fe18Cr34Ni are well above 15 cation % (see Table 3). Thus, the observed trend of Ni shifting the regions for D-IO ('BCC+S_{Cr}+FCC') to the left, implies that both these protective oxides would be outside of the D-IO region and that the expected phases for these alloys would also be S_{Cr}+FCC.

Hence, the average composition of the inward-growing scales formed on the poorly protective oxides are within the D-IO region, whereas the composition of the slow-growing oxides are outside of this region after both 48 and 168 h. Thus, it is suggested that a good secondary corrosion protection may be established only if the D-IO region may be avoided and not by internal oxidation overall, as opposed to the secondary corrosion protection formed on FeCrAl alloys. This may be achieved either by an increased amount of Cr, or by shifting the stability region to lower Cr-contents by the addition of Ni.

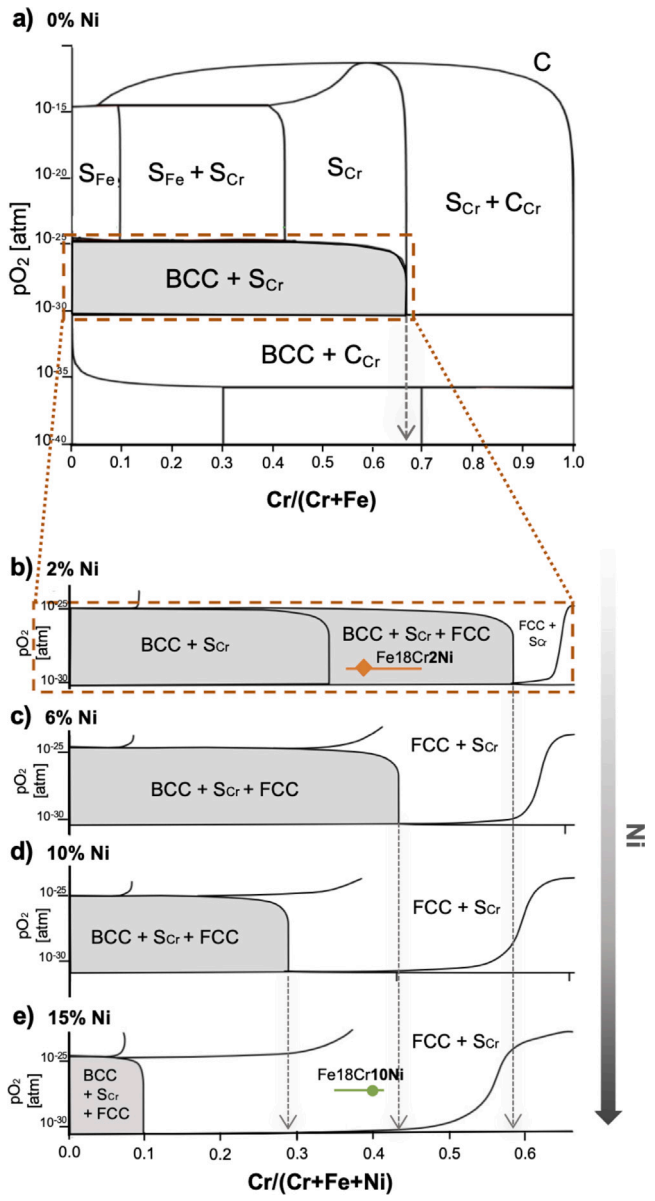

Fig. 6. Phase diagram for FeCrNi alloys at 600 °C showing the equilibrium phases at different pO_2 for varying Cr content while keeping a fixed amount of Ni: (a) 0%Ni (b) 2%Ni, (c) 6%Ni, (d) 10%Ni, (e) 15%Ni. Note that the markings of different alloy compositions only marks the approximate Cr-content in the spinel formed on specified alloys and not the exact pO_2-value.

4.4. Beyond internal oxidation

The main difference between the two types of internal oxidation (D-IO: 'BCC'S+FCC' and IO: 'S+FCC') is proposed to be that the Fe-rich BCC is rapidly oxidized, whereas the FeNi-FCC remains non-oxidized both in the alloys exhibiting poor and good secondary corrosion protection. This is simply explained by that the oxidation of Ni is not promoted at these low partial pressures of oxygen. Hence, the FeNi-metal regions remain non-oxidized. The explanation may be validated by the bright contrast regions (FeNi-metal) observed in Fig. 4.

Moreover, the evolution of both oxide microstructure and chemical composition between 48 and 168 h was modest for the investigated alloys (see Tables 2–3). The composition of the inward-growing scale formed on the alloys exhibiting good secondary protection evolved slightly more than the poorly protective oxides between 48 and 168 h of exposure, resulting in higher Cr-contents for the longer exposures. This is suggested to be explained by an increased amount of Cr-rich spinel (reduced amount of FeNi-metal) after the longer exposure. The suggestion is also strengthened by comparing the amount of bright contrast regions, associated with FeNi-metal, dispersed in the inward-growing scale (see Fig. 4) for samples exposed for 48 and 168 h respectively.

The poorly protective oxide scales contained a considerable amount of IO-pores, and only small amounts of remaining metal were visible in the scale (brighter regions in the BSE image in Fig. 4b). This is in good agreement with the phase fractions calculated in the position marked for Fe18Cr2Ni (see Fig. 6a), resulting in approximately 65% spinel (chromite: 67 cation% Cr), 34% BCC, 1% FCC. Note that the amount of BCC is reduced for higher Cr contents (further to the right in the phase diagram in the same IO-region), while more Cr-rich spinel is formed. In contrast, the alloy exhibiting good secondary corrosion protection contained less IO-pores but considerably more remaining metal regions in the inward-growing scale (see Fig. 4), which would also be predicted by the phase diagram in Fig. 6 (more FCC).

5. Conclusion

To conclude; the corrosion protection of FeCrNi alloys after breakaway is clearly influenced by the amount of Ni in the alloy at 600 °C. All investigated alloys form mainly diffusion controlled, multi-layered, Fe-rich oxide scales after breakaway. The Fe-rich oxide scales formed on alloys with low Ni contents (≤2 wt%) are poorly protective, with growth rates similar to low alloyed steels, whereas the higher Ni contents result in the formation of a more slow-growing, Fe-rich oxide scale, i.e., a good secondary corrosion protection. The results suggest that a good secondary corrosion protection may be obtained by avoiding detrimental internal oxidation (D-IO), i.e., internal oxidation including Fe-rich BCC + Cr-rich spinel (+FCC). This can be achieved by an increased amount of Cr, but also by increasing the amount of Ni, since the range of stability for this type of internal oxidation is shifted towards lower Cr contents as the amount of Ni is increased. Thus, the main influence that Ni exert on the oxide growth rate after breakaway is suggested to be to shift the stability region of internal oxidation including Fe-rich BCC and Cr-rich spinel. This results in that less Cr is required to escape this type of internal oxidation, which allows for the formation of a good secondary corrosion protection.

The good secondary protection of FeCrNi alloys is reached above a critical amount of Ni (2% ≤ 10% for Fe**18Cr**xNi alloys), while additional Ni makes only a minor difference in oxide growth rate for the environment studied. However, thermodynamic equilibrium calculations indicate that, given time, the Cr-rich spinel oxide formed after breakaway could transition into a Cr-rich corundum-type oxide. Thus, it is suggested that the secondary corrosion protection formed after breakaway acts as a pre-step for the formation of a protective thick Cr-rich corundum type oxide. Moreover, the increased Cr-activity for higher amounts of Ni in the austenitic alloys could accelerate the formation of such a Cr-rich oxide after breakaway. If this would form below an outward-growing Fe oxide, it would in addition naturally reduce the risk for future breakaway events caused by reactions with the Cr-rich oxide.

CRediT authorship contribution statement

A. Persdotter: Writing – review & editing, Writing – original draft, Visualization, Validation, Supervision, Project administration, Methodology, Investigation, Data curation, Conceptualization. **H. Larsson:** Writing – review & editing, Software, Methodology. **J. Eklund:** Writing – review & editing, Methodology. **S. Bigdeli:** Writing – review & editing, Software, Methodology. **T. Jonsson:** Funding acquisition, Project administration, Supervision, Writing – review & editing.

Declaration of competing interest

The authors declare that they have no known competing financial interests or personal relationships that could have appeared to influence the work reported in this paper.

Data availability

Data will be made available on request.

Acknowledgments

This work was carried out within the High Temperature Corrosion Centre (HTC) at Chalmers University of Technology, and with support from VINNOVA, Sweden, Sweden's Innovation Agency, within the Metallic Materials program, that are hereby gratefully acknowledged together with the Swedish Energy Agency and project member companies (Alleima AB, Kanthal AB, Thermo-Calc Software AB, Energiforsk AB, Vattenfall, Sweden, Eon, Öresundskraft, Babcock and Wilcox Volund A/S, MH Engineering AB, Valmet Technologies Oy, Sumitumo SHI FW Energia Oy, Babcock and MEC BioHeat and Power A/S, Sweden). The research was performed in part at the Chalmers Materials Analysis Laboratory, CMAL. The authors acknowledges William Phung for performing exposures and analysis during his thesis work at Chalmers university of technology.

References

[1] P. Kofstad, High Temperature Corrosion, Elsevier Applied Science, 1988.
[2] D.J. Young, High Temperature Oxidation and Corrosion of Metals, second ed., Elsevier, 2016.
[3] A. Persdotter, J. Eklund, J. Liske, T. Jonsson, Beyond breakaway corrosion - influence of chromium, nickel and aluminum on corrosion of iron-based alloys at 600 °C, Corros. Sci. (177) (2020).
[4] G.C. Wood, D.P. Whittle, The mechanism of breakthrough of protective chromium oxide scales on Fe-Cr alloys, Corros. Sci. 7 (11) (1967).
[5] M.G. Hobby, The role of nickel in the high-temperature oxidation of Fe-Cr-Ni alloys in oxygen, Oxid. Met. 1 (1) (1969) 23–54.
[6] H. Asteman, J. Svensson, M. Norell, L. Johansson, Influence of water vapor and flow rate on the high-temperature oxidation of 304L ; effect of chromium oxide hydroxide evaporation, Oxid. Met. 54 (1–2) (2000) 11–26.
[7] H. Asteman, K. Segerdahl, J.E. Svensson, L.G. Johansson, The influence of water vapor on the corrosion of chromia-forming steels, Mater. Sc. Forum 369–372 (I) (2001) 277–286.
[8] R. Peraldi, B.A. Pint, Effect of Cr and Ni contents on the oxidation behavior of ferritic and austenitic model alloys in air with water vapor, Oxid. Met. 61 (5–6) (2004) 463–483.
[9] J. Ehlers, D.J. Young, E.J. Smaardijk, A.K. Tyagi, H.J. Penkalla, L. Singheiser, W.J. Quadakkers, Enhanced oxidation of the 9%Cr steel P91 in water vapour containing environments, Corros. Sci. 48 (11) (2006) 3428–3454.
[10] J. Pettersson, H. Asteman, J.E. Svensson, L.G. Johansson, KCl induced corrosion of a 304-type austenitic stainless steel at 600 degrees C; the role of potassium, Oxid. Met. 64 (1–2) (2005) 23–41.
[11] F. Liu, J.E. Tang, T. Jonsson, S. Canovic, K. Segerdahl, J.E. Svensson, M. Halvarsson, Microstructural investigation of protective and non-protective oxides on 11% chromium steel, Oxid. Met. 66 (5–6) (2006) 295–319.
[12] T. Jonsson, F. Liu, S. Canovic, H. Asteman, J.-E. Svensson, L.-G. Johansson, M. Halvarsson, Influence of H_2 O(g) on the oxide microstructure of the stainless steel 353MA at 900 ° C in oxygen, J. Electrochem. Soc. 154 (11) (2007) C603.
[13] E. Essuman, G.H. Meier, J. Zurek, M. Hänsel, L. Singheiser, W.J. Quadakkers, Enhanced internal oxidation as trigger for breakaway oxidation of Fe-Cr alloys in gases containing water vapor, Scr. Mater. 57 (9) (2007) 845–848.
[14] C. Pettersson, L.G. Johansson, J.E. Svensson, The influence of small amounts of KCl(s) on the initial stages of the corrosion of alloy sanicro 28 at 600 degrees C, Oxid. Met. 70 (5–6) (2008) 241–256.
[15] T. Jonsson, J. Froitzheim, J. Pettersson, J.E. Svensson, L.G. Johansson, M. Halvarsson, The influence of KCl on the corrosion of an austenitic stainless steel (304L) in oxidizing humid conditions at 600 °C: A microstructural study, Oxid. Met. 72 (3–4) (2009) 213–239.
[16] N.K. Othman, J. Zhang, D.J. Young, Water vapour effects on Fe-Cr alloy oxidation, Oxid. Met. 73 (1–2) (2010) 337–352.
[17] A.N. Hansson, K. Pantleon, F.B. Grumsen, M.A. Somers, Microstructure evolution during steam oxidation of a Nb stabilized austenitic stainless steel, Oxid. Met. 73 (1–2) (2010) 289–309.
[18] J. Pettersson, N. Folkeson, L.-G. Johansson, J.-E. Svensson, The effects of KCl, K_2SO_4 and K_2CO_3 on the high temperature corrosion of a 304-type austenitic stainless steel, Oxid. Met. 76 (2011) 93–109.
[19] B. Pujilaksono, T. Jonsson, H. Heidari, M. Halvarsson, J.E. Svensson, L.G. Johansson, Oxidation of binary FeCr alloys (Fe-2.25Cr, Fe-10Cr, Fe-18Cr and Fe-25Cr) in O_2 and in O_2 + H_2O environment at 600 °c, Oxid. Met. 75 (3–4) (2011) 183–207.
[20] T. Gheno, D. Monceau, D.J. Young, Mechanism of breakaway oxidation of Fe – Cr and Fe – Cr – Ni alloys in dry and wet carbon dioxide, Corros. Sci. 64 (2012) 222–233.
[21] N. Mu, K.Y. Jung, N.M. Yanar, G.H. Meier, F.S. Pettit, G.R. Holcomb, Water vapor effects on the oxidation behavior of fe-cr and Ni-Cr alloys in atmospheres relevant to oxy-fuel combustion, Oxid. Met. 78 (3–4) (2012) 221–237.
[22] L. Liu, Z.-G. Yang, M. Zhang, K. Kawamura, T. Maryama, Effect of water vapour on the oxidation of Fe-13Cr-5Ni martensitic alloy at 973 K, Corros. Sci. 60 (2012) 90–97.
[23] J. Lehmusto, B.-J. Skrifvars, P. Yrjas, M. Hupa, Comparison of potassium chloride and potassium carbonate with respect to their tendency to cause high temperature corrosion of stainless 304L steel, Fuel Process. Technol. 105 (2013) 98–105.
[24] T. Jonsson, B. Pujilaksono, H. Heidari, L. F., J.-E. Svensson, M. Halvarsson, L.-G. Johansson, Oxidation of Fe-10Cr in O_2 and in O_2+H_2O environment at 600 °C: A microstructural investigation, Corros. Sci. 75 (2013) 326–336.
[25] A. Col, V. Parry, C. Pascal, Oxidation of a Fe–18Cr–8Ni austenitic stainless steel at 850 °C in O_2: Microstructure evolution during breakaway oxidation, Corros. Sci. 114 (2017) 17–27.
[26] T. Jonsson, H. Larsson, S. Karlsson, H. Hooshyar, M. Sattari, J. Liske, J.E. Svensson, L.G. Johansson, High-temperature oxidation of FeCr(Ni) alloys: The behaviour after breakaway, Oxid. Met. 87 (3–4) (2017) 333–341.
[27] F.J. Frandsen, Utilizing biomass and waste for power production - a decade of contributing to the understanding, interpretation and analysis of deposits and corrosion products, Fuel 84 (10) (2005) 1277–1294.
[28] J. Pettersson, J.-E. Svensson, L.-G. Johansson, Alkali induced corrosion of 304-type austenitic stainless steel at 600 °C; comparison between KCl, K_2CO_3 and K_2SO_4, Mater. Sci. Forum 595-598 PA (2008) 367–375.
[29] T. Jonsson, S. Karlsson, H. Hooshyar, M. Sattari, J. Liske, J.-E. Svensson, L.-G. Johansson, Oxidation after breakdown of the chromium-rich scale on stainless steels at high temperature : Internal oxidation, Oxid. Met. 85 (2016) 509–536.
[30] S. Mori, T. Sanusi, N. Simms, J. Sumner, Fireside corrosion and deposition on heat exchangers in biomass combustion systems, Mater. High Temp. 40 (1) (2023) 36–47, [Online]. Available: https://doi.org/10.1080/09603409.2022.2138007.
[31] A.N. Hansson, M. Montgomery, M.A. Somers, Development of the inner oxide zone upon steam oxidation of an austenitic stainless steel, Mater. High Temp. 26 (1) (2009) 39–44.
[32] J. Eklund, B. Jönsson, A. Persdotter, J. Liske, J. Svensson, T. Jonsson, The influence of silicon on the corrosion properties of FeCrAl model alloys in oxidizing environments at 600 °C, Corros. Sci. 144 (2018) 266–276.
[33] J. Eklund, A. Persdotter, V. Ssenteza, T. Jonsson, The long-term corrosion behavior of fecral(Si) alloys after breakaway oxidation at 600 °C, SSRN Electron. J. 217 (November 2022) (2023) 111155, [Online]. Available: https://doi.org/10.1016/j.corsci.2023.111155.
[34] J. Eklund, A. Persdotter, I. Hanif, S. Bigdeli, T. Jonsson, Secondary corrosion protection of FeCr(Al) model alloys at 600 °C – the influence of Cr and Al after breakaway corrosion, Corros. Sci. 189 (May) (2021) 109584, [Online]. Available: https://doi.org/10.1016/j.corsci.2021.109584.
[35] V. Ssenteza, J. Eklund, S. Bigdeli, T. Jonsson, Long-term corrosion behavior of FeCr(Al, Ni) alloys in O_2 + H_2O with KCl(s) at 600 °C: Microstructural evolution after breakaway oxidation, Corros. Sci. 226 (111654) (2024).
[36] J. Andersson, T. Helander, L. Höglund, P. Shi, B. Sundman, Thermo-calc and DICTRA, computational tools for materials science, CALPHAD 26 (2002) 273–312.
[37] R.F.A. Pettersson, J. Enecker, L. Liu, Role of nickel in the oxidation of Fe-Cr-Ni alloys in air-water vapour atmospheres, Mater. High Temp. 22 (3–4) (2005) 269–281.
[38] R.F.A. Pettersson, Effects of composition on the corrosion of Fe-Ni-Cr alloys in chlorinating and sulfidising environments, Mater. High Temp. 26 (3) (2009) 217–222.